ANALYTICAL AND NUMERICAL MODELLING OF OSMOTICALLY INDUCED DEFORMATION IN A SPHERICAL CELL

Jake Bewick

Abstract

Determining cell stiffness has become a routine practice in the study of mechanotransduction and cellular modelling, with the most popular method currently being atomic force microscopy (AFM). Unfortunately, AFM is limited by the formation of a water meniscus, the need for specialised equipment, and the inability to process multiple cells simultaneously.

This report derives the governing equations behind a new, potential alternative to AFM. A cell is modelled as a poroelastic material encapsulated in a partially permeable membrane, across which we can use a hypo/hyperosmotic solution to generate an osmotic gradient. The resulting flux of water causes the cells to swell or shrink, with the degree of deformation being dependent on the cell's stiffness, Poisson's ratio, and permeability.

The governing partial differential equation was solved using the Laplace transform to create a solvable ordinary differential equation, following which the Cauchy residue theorem was used to return to the time domain. For validation we also use Talbot's method to numerically compute the inverse Laplace transform and create a separate simulation of swelling using ABAQUS.

Dimensionless solutions of pore pressure and displacement as a function of radius and time are provided. Critically, the surface settlement of a swelling cell has been calculated – such swelling can easily be recorded *in vitro* on any standard microscope and fit against the provided model to calculate the mechanical properties of the cell in question.

Contents

Acknowledgements

The author would like to thank his personal supervisor, Profesor Ventikos for his guidance and advice over the past year. His insights into poroelasticity were invaluable. I would also like to thank Professor Jayasinghe for use of his lab.

1 List of Symbols

Symbol	Name	Units
R	Radius	m
R_0	Initial radius	m
R^*	Dimensionless radius	-
θ	Polar angle	rad
φ	Azimuthal angle	rad
t	Time	s
t^*	Dimensionless time	-
σ	Stress	Pa
σ_{RR}	Radial stress	Pa
$\sigma_{\theta\theta} = \sigma_{\varphi\varphi}$	Tangential stress	Pa
σ_{ij}	Cauchy stress tensor	Pa
e	Total volumetric strain	-
e_{ij}	Infitesimal strain tensor	-
$e_\theta = e_\varphi$	Tangential strain	-
u	Displacement	m
u_R	Radial displacement	m
$u_\theta = u_\varphi$	Tangential displacement	m
p	Pore pressure	Pa
P_0	Initial pressure	Pa
s	Complex frequency	-
s^*	Dimensionless complex frequency	-
λ	First Lam\'{e} constant	Pa
λ_u	Undrained first Lam\'{e} constant	Pa
μ	Second Lam\'{e} constant	Pa
ζ	Volumetric variation in fluid content	-
A, A'	Undefined temporary constants	-
M	Biot modulus	Pa
α	Biot effective stress coefficient	-
G	Shear modulus	Pa
ν	Poisson's ratio	-
η	Poroelastic stress coefficient	-
c	Consolidation coefficient	-
S	Storage coefficient	-
B	Skempton pore pressure coefficient	-
κ	Permeability	m^2
Π	Osmotic Pressure	Pa
i	van't Hoff factor	-
$\mathcal{C}$	Molar concentration	mol/L
$\mathcal{R}$	Ideal gas constant	$JK^{-1}mol^{-1}$
$\mathcal{T}$	Temperature	K

2 List of Tables

3 List of Figures

4 Introduction

4.1 Measuring Cell Stiffness

Most biological tissues have an inherently hierarchical structure [1]: macroscale mechanical properties are largely governed by microscale cells and the extracellular matrix they produce. Mechanically aberrant biological tissue is both an indication of, and cause of many diseases [2] - specifically, increased tissue stiffness can lead to polycyctic kidney disease [3], cancer metastasis [4] and other afflictions (see review by Jaalouk and Lammerding [5]). It is unsurprising that researchers are motivated to study the mechanics of individual cells, and as such many different techniques have arisen to allow for that.

Atomic force microscopy, invented by Bennig in 1986 [6], is the most popular method for -quite literally- probing the mechanical properties of cells [7]. AFM was originally invented as an alternative to optical or current based (e.g. electron microscopy) imaging techniques [8]; the general principle behind AFM is that a nanoscale tip on a thin cantilever trawls across the surface of a sample, moving up and down over any corresponding peaks and troughs, recording the surface topography [9].

Aside from its imaging mode, AFM has been adapted to quantify the stiffness of cells [10]. Now the cantilever tip presses down into a sample, with the recorded displacement of the cantilever head being determined by interactions between tip and cell surface [11]. Mathematical models specific to tip geometry are then used quantify mechanical properties, such as stiffness, based on measured parameters (e.g. the Hertz model is used for spherical tips [12] while the Sneddon model is used for cone punches [13]).

Note that these mathematical models underlying AFM are based on critical assumptions that may not always be valid. For the Hertz model alone, the spherical tip head must both be much larger that the indentation depth [14] and not be significantly harder that the sample [15]. This means that for a inhomogeneous sample there may only be specific regions where the model is valid.

AFM is very slow compared to other imaging techniques - a possible limitation when applied to cells which tend to relax and spread over time. Much like the Rayleigh criterion limits optical resolution, the undampened vibrations of a high-speed scanning probe introduce a scan speed limit on AFM [16]. Advances in the last two decades have pushed this limit, high resonance frequency cantilevers [17], microresonators [18] and ultra-high speed imaging devices [19] have seen high-speed AFM "*come of age*" [20].

Unfortunately these proposed solutions are only imaging a small region of a relatively larger specimen - AFM must scan through these local regions in series to capture a complete working stiffness map of a cell. Parallelisation has been attempted to overcome this problem [21, 22], however that just exacerbates another limitation with AFM

- its prohibitive cost.

AFM requires expensive equipment, prolonged set-up and meticulous calibration. Mechanotransduction remains a nascent field, with many researches attempting to pique greater interest in cellular mechanics among the wider biologist community [23] - AFM remains a limitation in achieving that aim. An ideal alternative would use materials and equipment already readily available in most labs.

Existing alternatives to AFM include optical and magnetic tweezers, elastomeric microposts and integrated strain arrays. Each will be briefly addressed below.

Optical tweezers are a versatile method of assessing stiffness, able to exert piconewton force on nano or micro sized particles and measure the subsequent displacement [24]. A silica bead is attached to the surface of a cell [25], a focused beam of laser light creates a "trap" on the dielectric bead, drawing it the the centre of the trap [26]. The actual displacement of the bead is dependent on the mechanical properties of the cell. Optical tweezers have been successfully used not just to determine linear elastic mechanical properties but also non-linear and viscoelastic properties of cells [27]. Unfortunately it has been discovered that the laser light used to optically trap particles can heat the cell, potentially damaging it [28]. Furthermore, optical tweezers are non-specific, they trap any dielectric particle [24] - even cell organelles have been trapped [29].

Magnetic tweezers are similar to optical tweezers, except a magnetic field is used to exert a force on paramagnetic beads applied to the surface of the cell. Magnetic tweezers are capable of exerting nanonewton forces on cells, and (unlike optical tweezers) can apply torque by rotation of the magnetic field [24]. However it is much more difficult to produce a focused and significantly powerful magnetic field as oppossed to optical trap techniques [24].

Mechanical sensing using elastomeric microposts attach cells onto the surface of an array of micron sized silicon pillars. A vacuum is used to apply stretch forces to the pillars, deforming the attached cell with the degree of deformation being proportional to cell stiffness [30]. Unfortunately cells do not attach ideally to pillars, integrin clustering often occurs that can disturb force transmission [31].

Integrated strain arrays function by depositing cells on a biocompatible polymer membrane, which can then be stretched over a polymeric post to strain the attached cell [32]. Unlike the elastomeric micropost method, integrated strain arrays present a flat surface over which cells can adhere. However, quantification of cellular mechanical properties has not been achieved with this technique, instead it is just method to apply a controllable amount of strain during cell culture.

Regarding these methods of cell stiffness measurement as a whole it becomes clear there are many common disadvantages. As such we outline our requirements for a new alternative method that motivate the remainder of the report.

The proposed method should:

1. be capable of quantifying cellular mechanical properties.
2. require equipment typically found in most labs.
3. be quick.
4. assess several cells in tandem.
5. not damage the cell.
6. not allow for cell adhesion.

4.2 Osmotically Induced Deformation of a Spherical Cell

In this report we propose modelling a cell as a linear elastic poroelastic sphere - a geometry that is easily achievable following trypsinization [33]. Like with most other quantification methods, we then apply a controllable force to the cell and measure the resultant displacement - in this case measuring the change in radius of the cell through a standard microscope. The degree of deformation would then be inversely proportional to the stiffness of the cell.

Poroelastic materials consist of a porous solid phase (representing the cytoskeleton, organelles, macromolecules etc.) and a interstitial fluid phase (the cytosol) that saturates the material [34]. Although the two phases interact, they are ultimately their own materials, with separate mechanical properties. In poroelasticity, loads can be independently applied directly to the solid skeleton as stress or on the fluid phase as pore pressure.

Cells themselves can be reliably considered as poroelastic materials, in 2013 Moeendarbary *et al.* used a poroelastic model of cytoplasm to successfully model cell rheology [34]. Poroelastic modelling has also been used to model cell crawling [35] and stress relaxation in chondrocytes [36].

This thesis proposes three different methods for loading the cells, and presents the governing equations behind each.

The first loading method, referred to as "Mode 1", involves directly loading the solid skeleton. A mechanical force is applied uniformly across the surface of the sphere with fluid being free to drain through this surface. This mode has a special name, known as

"Cryer's problem" and has been analytically solved for over half a decade [37].

In the second loading mode there is no strain applied to the solid skeleton. Instead we apply a pore pressure to the surface of the cell, and measure the subsequent swelling or shrinkage. This pore pressure can either be applied hydrostatically or by generating an osmotic gradient across a partially permeable membrane (in this case the phospholipid bilayer). We recommend generating this force osmotically as no special equipment is needed to load the cell - it is trivial to prepare a hypoosmotic or hyperosmotic solution in any lab. While the fundamental constitutive equations of poroelasticity remain unchanged from Cryer's problem the change in boundary conditions leads to a completely unique solution that has been derived in this thesis.

The final loading mode involves loading a cell using fluid pressure, both the solid skeleton and interstitial fluid are loaded simultaneously. This loading mode is merely a superposition of the two previous loading modes.

In this thesis we derive the analytical solution to the different loading modes and present graphs of the expected dimensionless change in pore pressure and displacement as a function of radial distance and time. For validation, we compare the analytical solution with a numerical solution and computational simulation.

5 Consolidation of a Poroelastic Sphere

5.1 Cryer's Problem

A thoroughly studied problem in poroelasticity is that of one-dimensional consolidation - a soil layer resting on an impermeable base is compressed by a load, with fluid able to freely drain from the surface of the soil. The evolving pore pressure, stresses and strains within the soil were solved analytically by Terzhagi in a series of six papers [38], leading to the emergence of an entire new field of engineering - geotechnical engineering [39]. Within this field the solution is ubiquitous [38], Terzaghi's work is regularly used by practising geotechncial engineers and forms a key part of any undergraduate course. Moreover, it is regularly used for validating new numerical techniques [40].

Terzhagi's problem has also been solved in spherical coordinates under the assumption of spherical symmetry by Cryer [37]. A load is applied on the surface of a poroelastic sphere with free draining possible. Although less well known than Terzaghi's original work, Cryer's solution has seen both theoretical and practical applications (we focus on specifically biological applications) that are briefly addressed in Table 1.

Table 1: Theoretical and Practical Applications of Cryer's Problem

Theoretical Applications	Practical Applications (Biological)
• Cryer originally only solved for pore pressure at the centre of the sphere and the surface settlement. Comprehensive solutions of pore pressure, stress and strain across the entire radius were solved 30 years layer by Mason *et al.* [41] • Both Cryer and Mason consider the fluid and solid phases as incompressible. The general solution is presented in textbooks by Cheng [43] and Verruijt [44]. • Cryer's solution has recently been expanded to encompass N-layer spheres with different porosities and permeabilities for each layer [46]. • Gibson *et al.* have studied Cryer's problem under large displacements, noting that the Mandel-Cryer effect still occurs with large strains [47].	• Nowinski and Davis expand on Cryer's solution to create an analytical model of the human skull modelled as a poroelastic shell. They stress their model and find a good match with existing rheological models of human bone. [42]. • Islam and Righetti have used Cryer's work to create a model of creep compression of a tumour compressed between two plates [45].

5.2 Problem Definition

5.2.1 Loading By Stress

The governing equations describing poroelastic consolidation are formulated as differential equations. As such a set of boundary conditions are needed to find the solution. In Cryer's problem (mode 1) we begin by defining a sphere with radius R_0. In this report we wish to solve for pore pressure (p) and displacement (u) as a function of both time (t) and radius (R) where $0 \leq t < \infty$ and $0 \leq R \leq R_0$. As previously mentioned we know that a pressure (P_0) is applied at the surface of the sphere, as such the radial stress (σ_{RR}) at this location must be equal to this pressure. Furthermore pore pressure must be 0 so that fluid can freely drain through the surface of the sphere. Stated another way we reach our first set of boundary conditions:

$$\begin{aligned} \sigma_{RR} &= -P_0 H(t-0), \\ p &= 0, \\ \text{at } R &= R_0 \end{aligned} \tag{1}$$

Where $H(t-0)$ is the Heaviside step function, ensuring that there is no load applied when $t < 0$ and once $t > 0$ the load is both instantaneously applied and continuous.

Another set of boundary conditions exist that define displacement and pore pressure at the centre of the sphere, when $R = 0$. As the problem is axisymmetric there can be no deformation at the centre ($u_R = 0$). Similarly there is no change in pore pressure as a function of radius ($\frac{\partial p}{\partial R} = 0$). We can state this mathematically as:

$$\begin{aligned} u_R &= 0, \\ \frac{\partial p}{\partial R} &= 0, \\ \text{at } R &= 0 \end{aligned} \tag{2}$$

5.2.2 Loading by Pore Pressure

It is easy to imagine how stress may be applied to a poroelastic material in Terzhagi's problem, however the spherical geometry of Cryer's problem is more challenging as load must be applied evenly across the entire surface of the sphere.

As previously mentioned we could also deform the poroelastic cell by loading the interstitial fluid. Now the load is applied not on the the solid skeleton ($\sigma_{RR} = 0$), but instead as pore pressure at the surface of sphere ($p = P_0 H(t-0)$). While our second set of boundary conditions remains unchanged (Equation 2), the new loading necessitates a change in our first set of previously defined boundary conditions (see Equation 1):

$$\begin{aligned} \sigma_{RR} &= 0, \\ p &= P_0 H(t-0), \\ \text{at } R &= R_0 \end{aligned} \tag{3}$$

This pore pressure can be applied either hydrostatically or via osmosis if a partially permeable membrane is present. Using osmosis to generate pore pressure on the surface of the sphere is particularly attractive as an appropriate sample just needs to be placed in an osmotic medium.

The major application of this method, and the motivation of this thesis, would be the ability to model the osmotically induced deformation of cells using this method. A spherical cell (achievable via trypsinization) could be submerged in an easily prepared ionic solution, the osmotically induced flux of water across the partially permeable phospholipid bilayer membrane would cause the cell to swell or shrink based on solution tonicity and cell mechanical properties. The geometry of such a problem is show in Figure 1.

The osmotic pressure (Π) applied on a cell by a hypoosmotic or hyperosmotic medium can be trivially calculated from van't Hoff's equation of osmotic pressure in a dilute solution [43]:

$$\Pi = i\mathcal{C}\mathcal{R}\mathcal{T} \tag{4}$$

Where i is the van't Hoff factor, $\mathcal{C}$ is molar concentration, $\mathcal{R}$ is the ideal gas constant, and $\mathcal{T}$ is temperature.

Alternatively, if a strong hyperosmotic medium is required an aqueous solution of highly hydrophilic polyethylene glycol (PEG) can be prepared. Experimentally derived formulae to calculate the osmotic pressures of various PEG solutions have been found using vapour pressure deficit osmometry [48] and sedimentation equilibrium ultracentrifugation [49].

In this report we derive solutions for how pore pressure and strain change as a function of radius and time for both loading modes and present the ultimate superposition that describes fluid pressure loading.

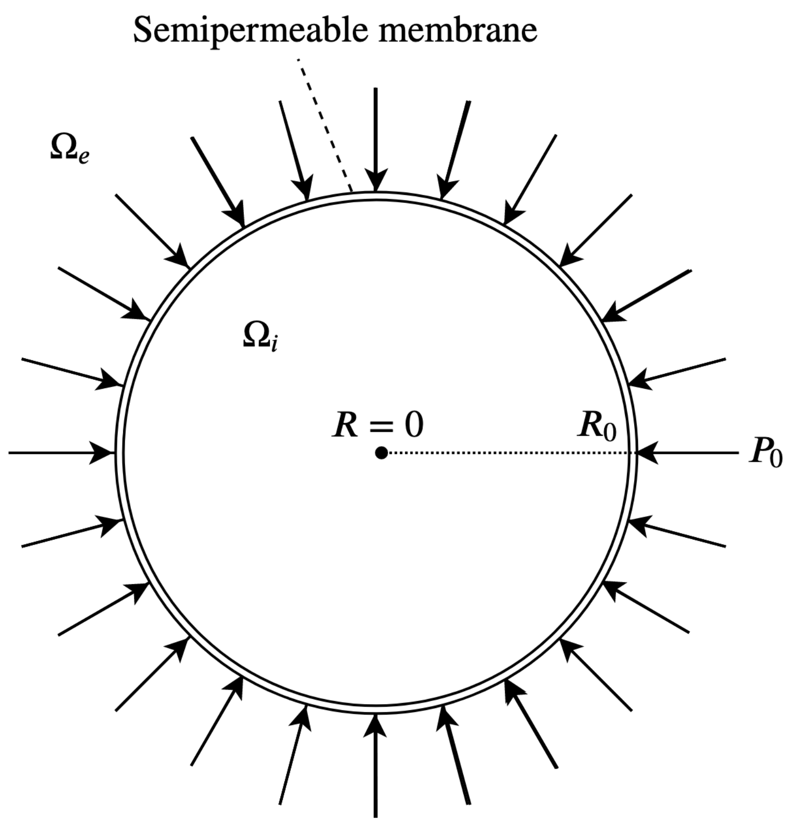

Figure 1: The osmotically induced deformation of a spherical cell Ω_i. A spherical trypsinized cell of radius R_0 is submerged in a a hypotonic or hypertonic medium Ω_e. This generates a pore pressure of P_0 at the surface of the sphere, causing the cell to swell or shrink. In this report we derive the equations governing this deformation, and the resulting change in pore pressure.

5.3 Governing Equation

The governing equations of poroelasticity are constitutive equations that link dynamic quantities (e.g. stresses) to kinematic quantities (e.g. strains) [43]. To formulate this relationship we begin by considering the well known stress-strain constitutive equation for a isotropic linear elastic material [50]:

$$\sigma_{ij} = \lambda \delta_{ij} e + 2\mu e_{ij} \tag{5}$$

Where σ_{ij} is the Cauchy stress tensor, e_{ij} is the infinitesimal strain tensor, e is the total volumetric strain, δ_{ij} is the Kronecker delta and λ and μ are the first and second Lamé parameters respectively. However, poroelastic materials consist of a porous solid phase and a fluid medium. As such the stress tensor is not just dependent on the strain tensor but also on the volumetric variation in fluid content ζ. Intuitively, this can be easily understood: if we compress a saturated porous material some of the fluid will drain during compression, and consequently the mechanical properties of the material will change. Equation 5 is now modified to incorporate this new term [43]:

$$\sigma_{ij} = \lambda_u \delta_{ij} e + 2\mu e_{ij} - A\delta_{ij}\zeta \tag{6}$$

Where λ now becomes specifically the undrained first Lamé parameter, λ_u, and A is a new constant - just like some materials may be stiffer than others, others may be more freely drained under compression (e.g. sand vs clay).

For now we have only considered a single dynamic quantity - the stresses on the solid grains. However a poroelastic material undergoing deformation also experiences a load applied to the fluid phase - a pore pressure p [43]:

$$p = -A'e + M\zeta \tag{7}$$

Where we define two new material constants, A' and M.

We can verify Equations 6 and 7 by checking they satisfy the Maxwell-Betti reciprocal work theorem. A comprehensive description of the process is provided by Cheng [43], but ultimately it is proven that $A = A'$ and as such both can be replaced by a single material constant. However it has been found more convenient to instead define A and A' as a product of M and the new constant α. We now have two Equations containing four material constants that are able to describe linearly elastic and isotropic poroelastic materials [43]:

$$\sigma_{ij} = \lambda_u \delta_{ij} e + 2\mu e_{ij} - \alpha M \delta_{ij}\zeta \tag{8}$$

$$p = M\left(-\alpha e + \zeta\right) \tag{9}$$

The two material constant, M and α are known the Biot modulus and the Biot effective stress coefficient respectively. It can be convenient to express the poroelastic constitutive equations as a single equation. We can do so by substituting Equation 9 into Equation 8 to find that [43]:

$$\sigma_{ij} = \lambda \delta_{ij} e + 2G e_{ij} - \alpha \delta_{ij} p \tag{10}$$

We define λ as the drained first Lamé parameter:

$$\lambda = \lambda_u - \alpha^2 M \tag{11}$$

Our cell is spherical, and consequently all governing equations are formulated in a spherical coordinate system (R, θ, φ), where R is the radial distance, θ is the polar angle and φ the azimuthal angle. As our geometry is assumed to be spherically symmetrical variables are functions of radial distance and time only.

Our poroelastic sphere does not experience an acceleration, and as such can be considered as a statics problem. Therefore it must satisfy the equilibrium equation stating that there are no net forces:

$$\sum \mathbf{F} = 0 \tag{12}$$

The equilibrium equations in spherical coordinates has been derived as [43]:

$$\frac{\partial \sigma_{RR}}{\partial R} + \frac{1}{R}\frac{\partial \sigma_{R\theta}}{\theta} + \frac{1}{R\sin\theta}\frac{\partial \sigma_{R\varphi}}{\partial \varphi} + \frac{1}{R}\left(2\sigma_{RR} - \sigma_{\theta\theta} - \sigma_{\varphi\varphi} + \sigma_{R\theta}\cot\theta\right) = 0 \tag{13}$$

$$\frac{\partial \sigma_{R\theta}}{\partial R} + \frac{1}{R}\frac{\partial \sigma_{\theta\theta}}{\theta} + \frac{1}{R\sin\theta}\frac{\partial \sigma_{\theta\varphi}}{\partial \varphi} + \frac{1}{R}\left[(\sigma_{\theta\theta} - \sigma_{\varphi\varphi})\cot\theta + 3\sigma_{R\theta}\right] = 0 \tag{14}$$

$$\frac{\partial \sigma_{R\varphi}}{\partial R} + \frac{1}{R}\frac{\partial \sigma_{\theta\varphi}}{\theta} + \frac{1}{R\sin\theta}\frac{\partial \sigma_{\varphi\varphi}}{\partial \varphi} + \frac{1}{R}\left(2\sigma_{\theta\varphi}\cot\theta + 3\sigma_{R\varphi}\right) = 0 \tag{15}$$

Owing to spherical symmetry many terms are eliminated, and the equilibrium equations instead reduce to just:

$$\frac{\partial \sigma_{RR}}{\partial R} + \frac{2\sigma_{RR} - \sigma_{\theta\theta} - \sigma_{\varphi\varphi}}{R} = 0 \tag{16}$$

$$\sigma_{\theta\theta} = \sigma_{\varphi\varphi} \tag{17}$$

And the dervied stress-strain relationship (Equation 10) becomes:

$$\sigma_{RR} = \lambda e + 2\mu e_{RR} - \alpha p \tag{18}$$

$$\sigma_{\varphi\varphi} = \lambda e + 2\mu e_{\varphi\varphi} - \alpha p \tag{19}$$

Where owing to spherical symmetry the various strains now become [43]:

$$e_{RR} = \frac{\partial u_R}{\partial R} \tag{20}$$

$$e_{\varphi\varphi} = e_{\theta\theta} = \frac{u_R}{R} \tag{21}$$

$$e = \frac{\partial u_R}{\partial R} + 2\frac{u_R}{R} = \frac{1}{R^2}\frac{\partial R^2 u_R}{\partial R} \tag{22}$$

Experimentally derived relationships between the Lamé parameters and more universally understood engineering constants (e.g. elastic, shear and bulk moduli) have been found [51]. As these engineering constants are more widely used by researchers we redefine our parameters in terms of shear modulus (G) and Poisson's ratio (v) using the following conversions [43]:

$$\lambda = \frac{2Gv}{1-2v} \qquad\qquad \mu = G \tag{23}$$

Consequently the constitutive equations now become:

$$\sigma_{RR} = \frac{2Gv}{1-2v}e + 2Ge_{RR} - \alpha p \tag{24}$$

$$\sigma_{\varphi\varphi} = \frac{2Gv}{1-2v}e + 2Ge_{\varphi\varphi} - \alpha \tag{25}$$

Note that although this thesis continues by using the shear modulus and Poisson's ratio, conversions exist for the elastic and bulk moduli [51]. Continuing on, Cheng substitutes in the stress-strain constitutive equations into the equilibrium equation to obtain the Navier equation [43]:

$$\frac{2G(1-v)}{1-2v}\left(\frac{\partial^2 u_R}{\partial R^2} + \frac{2}{R}\frac{\partial u_R}{\partial R} - \frac{2u_R}{R^2}\right) - \alpha\frac{\partial p}{\partial R} \tag{26}$$

Where we have defined one of many new poroelastic constants, the poroelastic stress coefficient, η [52]:

$$\eta = \frac{1-2v}{2(1-v)} \tag{27}$$

Much like the mechanical parameters characterising linear elasticity, conversion equations exist that allow researchers to restate any derived equation in terms of other poroelastic constants. Using the poroelastic stress coefficient is convenient however, as it allows us to rearrange Equation 26:

$$\frac{\partial e}{\partial R} = \frac{\partial}{\partial R}\left(\frac{1}{R^2}\frac{\partial R^2 u_R}{\partial R}\right) = \frac{\eta}{G}\frac{\partial p}{\partial R} \tag{28}$$

We can now integrate with respect to R to find [43]:

$$e = \frac{\eta}{G}p + 3A_1(t) \tag{29}$$

With A_1 being a new integration constant. We can integrate once more to find the solution for the strains [43]:

$$u_R(R,t) = \frac{\eta}{G}\frac{1}{R^2}\int R^2 p(R,t)dR + A_1(t)R + \frac{A_2(t)}{R^2} \tag{30}$$

Where A_2 is again another integration constant. These integration constants are found using the boundary conditions specific to each loading mode as will be seen later. We can substitute Equation 30 into the constitutive equations (Eq 18 & 19) to find the stress solutions [43]:

$$\sigma_{RR} = -4\eta \frac{1}{R^3} \int R^2 p(R,t) dR + \frac{2G(1+v)}{1-2v} A_1(t) - \frac{4G}{R^3} A_2(t) \tag{31}$$

$$\sigma_{\varphi\varphi} = 2\eta \frac{1}{R^3} \int R^2 p(R,t) dR - 2\eta p + \frac{2G(1+v)}{1-2v} A_1(t) - \frac{2G}{R^3} A_2(t) \tag{32}$$

Deriving a solution for radial and tangential stresses may seem unintuitive at first considering we are solving for pore pressure and displacement, however they are needed to eliminate certain integration constants as will become apparent later.

Deriving the governing equation for pore pressure is more involved and has not been comprehensively covered for brevity - once again the full derivation is provided by Cheng [43]. Stated briefly, it requires noticing that the displacement field under axisymmetric boundary conditions is irrotational. This allows Cheng to utilize a previously derived analytical solution for the pressure diffusion equation [43]:

$$\frac{\partial p}{\partial t} - c\nabla^2 p = -\frac{\eta(1-v)}{GS(1+v)} \frac{d}{dt} (\sigma_{kk} + 4\eta p) \tag{33}$$

Where c and S are new poroelastic constants called the consolidation coefficient and storage coefficient respectively.

He continues by noting that the term $\sigma_{kk} + 4\eta p$ is only a function of time. Therefore we can substitute in our previously derived stress solutions (Equations 31 and 32):

$$\sigma_{kk} + 4\eta p = \sigma_{RR} + 2\sigma_{\varphi\varphi} + 4\eta p = \frac{6G(1+v)}{1-2v} A_1(t) \tag{34}$$

We can substitute the above into the equation for pressure (Equation 33) to find:

$$\frac{\partial p}{\partial t} - c \frac{1}{R^2} \frac{\partial}{\partial R} \left(R^2 \frac{\partial p}{\partial R} \right) = -\frac{3\alpha}{S} \frac{dA_1(t)}{dt} \tag{35}$$

Which is a second-order partial differential equation governing pore pressure as a function of time and radius. Note that Equation 35 is just the diffusion equation in spherical coordinates with an extra term representing the integration constant, A_1. While we could solve this equation numerically using discretization techniques such as the finite difference method, such methods are often either conditionally or unconditionally unstable when applied to certain partial differential equations [53].

6 Loading By Stress

6.1 Laplace Transform

Instead we wish to solve Equations 30 and 35 analytically. To do so we begin by preforming a Laplace transform of the partial differential equation describing the change in pressure during consolidation (Equation 35), decomposing it into the following second-order non-homogeneous ordinary differential equation (ODE) [43]:

$$\frac{1}{R^2}\frac{\partial}{\partial R}\left(R^2\frac{\partial \tilde{p}}{\partial R}\right) - \frac{s}{c}\tilde{p} = \frac{3\alpha s}{\kappa}\tilde{A}_1(s) \tag{36}$$

Where κ is permeability, which has the following relationship with the consolidation and storage coefficients: [43]

$$\kappa = cS \tag{37}$$

The solution of this ODE is found to be [43]:

$$\tilde{p} = C_1\frac{\sinh\sqrt{R^2 s/c}}{R} + C_2\frac{\cosh\sqrt{R^2 s/c}}{R} - \frac{3\alpha}{S}\tilde{A}_1(s) \tag{38}$$

Note from the boundary conditions that the solution must be bounded at $R = 0$, as such C_2 must equal 0. If our geometry was instead a hollow sphere the complete solution is provided by Nowinski and David [42], the two researchers who modelled the skull as a poroelastic shell (see Table 1).

6.2 Pressure Solution

We first present Cryer's solution for pore pressure (mode 1). Throughout this report we make an assumption common in poroelastic modelling - that of incompressible constituents; we assume that the solid skeleton and interstitial fluid are both incompressible. The implications of this assumption will be discussed later in the thesis.

We can now proceed by using our first set of boundary conditions to solve for C_1 (see Equation 1, $p = 0$ when $R = R_0$) [43]:

$$0 = C_1\frac{\sinh\sqrt{R_0^2 s/c}}{R_0} - \frac{3\alpha}{S}\tilde{A}_1(s) \tag{39}$$

$$C_1 = \frac{3\alpha}{S}\tilde{A}_1(s)\left(\frac{R_0}{\sinh\sqrt{R_0^2 s/c}}\right) \tag{40}$$

We can now substitute Equation 40 into Equation 38 to find our pressure solution in the s-plane:

$$\tilde{p} = \frac{3\alpha}{S}\tilde{A}_1(s)\left(\frac{R_0\sinh\sqrt{R^2 s/c}}{R\sinh\sqrt{R_0^2 s/c}}\right) - \frac{3\alpha}{S}\tilde{A}_1(s) \tag{41}$$

$$\tilde{p} = -\frac{3\alpha}{S}\tilde{A}_1(s)\left(1 - \frac{R_0\sinh\sqrt{R^2 s/c}}{R\sinh\sqrt{R_0^2 s/c}}\right) \tag{42}$$

To remove the integration constant A_1 we recall our radial stress solution (Equation 31), noting that as before A_2 must equal 0 for stress to be bounded at $R = 0$. We substitute in our incomplete pressure solution (Equation 42) and integrate [43]:

$$\tilde{\sigma}_{RR} = -4\eta\frac{1}{R^3}\int R^2\tilde{p}(R,t)dR + \frac{2G(1+v)}{1-2v}\tilde{A}_1(s) \tag{43}$$

$$= -4\eta\frac{1}{R^3}\int \frac{3\alpha R^2}{S}\tilde{A}_1(s)\left(1 - \frac{R_0\sinh\sqrt{R^2 s/c}}{R\sinh\sqrt{R_0^2 s/c}}dR\right) + \frac{2G(1+v)}{1-2v}\tilde{A}_1(s) \tag{44}$$

$$= \Bigg[-\frac{24\eta^2(1-v)}{S(1-2v)}\frac{R^*\sqrt{s^*}\cosh(R^*\sqrt{s^*}) - \sinh(R^*\sqrt{s^*})}{{R^*}^3 s^*\sinh\sqrt{s^*}} \tag{45}$$

$$+ \frac{8\eta^2(1-v) + 2GS(1+v)}{S(1-2v)}\Bigg]\tilde{A}_1(s) \tag{46}$$

Where complex frequency, s, and radius, R, have been made dimensionless:

$$s^* = \frac{R_0^2 s}{c} \qquad\qquad R^* = \frac{R}{R_0} \tag{47}$$

We can now begin to apply our boundary condition that $\sigma_{RR} = -P_0H(t-0)$ when $R = R_0$ (Equation 1). Note that we are not substituting in radial stress in the time domain but instead the Laplace transformed equivalent, $\tilde{\sigma}_{RR}$. As such we must also find the Laplace transform of $-P_0H(t-0)$, which is just $-P_0/s$ as the Laplace transform of this variant of the Heaviside step function is $1/s$ [43]. Using this substitution we find [43]:

$$s\tilde{A}_1(s) = \frac{P_0S(1-2v)(v_u - v)s^*\sinh\sqrt{s^*}}{4\eta^2(1-v)D(s^*)} \tag{48}$$

Where we have eliminated the shear modulus from our equation using the relation:

$$G = \frac{2\eta^2(1-v)(1-v_u)}{S(v_u - v)} \tag{49}$$

And for shorthand we introduce $D(s^*)$:

$$D(s^*) = 6(v_u - v)\sqrt{s^*}\cosh\sqrt{s^*} - [6(v_u - v) + (1-v)(1+v_u)s^*]\sinh\sqrt{s^*} \tag{50}$$

We can now substitute in our result for $\tilde{A}_1(s)$ (Equation 48) into our incomplete pressure solution (Equation 42) to find our Laplace transformed pressure solution [43]:

$$\frac{s\tilde{p}}{P_0} = \frac{3(v_u - v)s^*}{2\eta D(s^*)R^*}\left[\sinh(R^*\sqrt{s^*} - R^*\sinh\sqrt{s^*})\right] \tag{51}$$

Recall that we are interested in the special case of incompressible constituents, for which the solid skeleton and interstitial fluid are assumed to be incompressible. Mathematically this implies that $v_u = 1/2$ and $\eta = (1-2v)/2(1-v)$. When these conditions are imposed, Equation 51 reduces to Equation 52 [37].

$$\frac{s\tilde{p}}{P_0} = \frac{s^*\left[\sinh(R^*\sqrt{s^*}) - R^*\sinh\sqrt{s^*}\right]}{R^*\left[4\eta\sqrt{s^*}\cosh\sqrt{s^*} - (s^* + 4\eta)\sinh\sqrt{s^*}\right]} \tag{52}$$

To find the solution to Equation 52 in the time domain we must preform an inverse Laplace transform. We note that Equation 52 is a ratio of two analytic function, meaning it has the form:

$$\tilde{f}_s = h(s)/g(s) \tag{53}$$

This means we can apply a variant of the Cauchy residue theorem to return to the time domain.

$$f(t) = \frac{1}{2\pi i}\int_{\gamma - i\infty}^{\gamma + i\infty}\tilde{f}(s)e^{st}ds = \frac{1}{2\pi i}\oint_C \frac{h(s)}{g(s)}e^{st}ds = \sum_{i=1}^{n}\frac{h(s_i)}{g'(s_i)}e^{s_i t} \tag{54}$$

Where the poles $s_i, i = 1, 2, ...n$ are found at the roots of the denominator of $g(s)$. In our equation the roots of the denominator can be found from the function $D(s^*)$, which we set equal to zero [43]:

$$\tanh\sqrt{s_n} = \frac{6(v_u - v)\sqrt{s_n}}{6(v_u) + (1-v)(1+v_u)s_n} \tag{55}$$

From the Cauchy integral theorem (Equation 54) we are then able to find the inverse Laplace transform by summing the residues at the poles [43]:

$$\frac{p(R,t)}{P_0} = \sum_{n=1}^{\infty}\frac{18(v_u - v)^2}{\eta E(s_n)}\left[\frac{\sinh(R^*\sqrt{s_n})}{R^*\sinh\sqrt{s_n}}\right]e^{s_n t^*} \tag{56}$$

Where for convenience, we define:

$$E(s_n) = -(1-v)^2(1+v_u)^2 s_n - 18(1+v)(v_u - v)(1 - v_u) \tag{57}$$

And introduce dimensionless time:

$$t^* = \frac{ct}{R_0^2} \tag{58}$$

As $s_n \geq 0$ we know that there is an imaginary argument for our hyperbolic functions [43]. Knowing that:

$$\sinh ix = i \sin x \qquad\qquad \cosh ix \cos x \tag{59}$$

We are able to remove the imaginary components from cosh and sinh. As a result s_n is replaced with $-x_n$. We find [43]:

$$\frac{p(R,t)}{P_0} = \sum_{n=1}^{\infty} \frac{18(v_u - v)^2}{\eta E(x_n)} \left[\frac{\sin(R^* \sqrt{x_n})}{R^* \sin \sqrt{x_n}} \right] e^{-x_n t^*} \tag{60}$$

Where:

$$E(x_n) = (1-v)^2(1+v_u)^2 x_n - 18(1+v)(v_u - v)(1 - v_u) \tag{61}$$

And now:

$$0 = \frac{6(v_u - v)\sqrt{x_n}}{6(v_u - v) - 1(1-v)(1+v_u)x_u} - \tan \sqrt{x} \tag{62}$$

For the previously discussed impressible constituents case we find [43]:

$$\frac{p(R,t)}{P_0} = \sum_{n=1}^{\infty} \frac{4(1-v)(1-2v)\left[\sin(R^* \sqrt{x_n}) - R^* \sin \sqrt{x_n}\right]}{\left[(1-v)^2 x_n - 2(1+v)(1-v)\right] R^* \sin \sqrt{x_n}} e^{-x_n t^*} \tag{63}$$

And:

$$0 = \frac{2(1-2v)\sqrt{x_n}}{2(1-2v) - (1-v)x_n} - \tan \sqrt{x_n} \tag{64}$$

6.3 Displacement Solution

Recall the previously derived solution for displacement (Equation 30), restated here:

$$u_R(R,t) = \frac{\eta}{G} \frac{1}{R^2} \int R^2 p(R,t) dR + A_1(t) R + \frac{A_2(t)}{R^2} \tag{65}$$

We preform the Laplace transform to find [43]:

$$\tilde{u}_R(R,s) = \frac{\eta}{G} \frac{1}{R^2} \int R^2 \tilde{p}(R,s) dR + \tilde{A}_1(s) R + \frac{\tilde{A}_2(s)}{R^2} \tag{66}$$

We know that $\tilde{A}_2 = 0$ and $\tilde{A}_1$ has been found to be (Equation 48):

$$s\tilde{A}_1(s) = \frac{P_0 S(1-2v)(v_u - v)s^* \sinh \sqrt{s^*}}{4\eta^2(1-v)D(s^*)} \tag{67}$$

And $\tilde{p}$ has been previously found to be (Equation 42):

$$\tilde{p} = -\frac{3\alpha}{S} \tilde{A}_1(s) \left(1 - \frac{R_0 \sinh \sqrt{R^2 s/c}}{R \sinh \sqrt{R_0^2 s/c}} \right) \tag{68}$$

We are now able to solve Equation 65 by making the appropriate substitutions to find:

$$\begin{aligned}\frac{s\tilde{u}_R}{u_R(R_0,\infty)} = R^* - \frac{3(v_u - v)}{(1-2v)D(s^*)R^{*2}} \Big\{ & 2(1-v)R^{*3}\sqrt{s^*}\cosh\sqrt{s^*} \\ & - \left[2(1-2v) + (1-v)s^*\right] R^{*3} \sinh\sqrt{s^*} \\ & + (1+v)\left[R^*\sqrt{s^*}\cosh(R^*\sqrt{s^*}) - \sinh(R^*\sqrt{s^*})\right]\Big\}\end{aligned} \tag{69}$$

Where:

$$u_R(R_0,\infty) = -\frac{P_0 R_0 (1-2v)}{2G(1+v)} \tag{70}$$

By applying the Cauchy residue theorem Cheng finds the solution in the time domain [43]:

$$\begin{aligned}\frac{\tilde{u}_R}{u_R(R_0,\infty)} = R^* - \sum_{n=1}^{\infty} & \frac{12(1+v)(v_u - v)}{(1-2v)E(x_n)R^{*2}x_n \sin\sqrt{x_n}} \\ & \times \Big\{3(v_u - v)\left[\sin(R^*\sqrt{x_n}) - R^*\sqrt{x_n}\cos(R^*\sqrt{x_n})\right] \\ & + (1+v)(1-2v)R^{*3}x_n \sin\sqrt{x_n}\Big\} e^{-x_n t^*}\end{aligned} \tag{71}$$

Under the assumption of incompressible constituents, this reduces to:

$$\begin{aligned}\frac{\tilde{u}_R}{u_R(R_0,\infty)} = R^* - \sum_{n=1}^{\infty} & \frac{4(1+v)(1-2v)}{\left[(1-v)^2 x_n - 2(1+v)(1-2v)\right] R^{*2} x_n \sin\sqrt{x_n}} \\ & \times \left[\sin(R^*\sqrt{x_n}) - R^*\sqrt{x_n}\cos(R^*\sqrt{x_n})\right] e^{-x_n t^*}\end{aligned} \tag{72}$$

7 Loading by Pore Pressure

7.1 Pressure Solution

We begin with our previously solved ordinary differential equation for pressure in the complex frequency domain (Equation 38). It is restated below to improve readability.

$$\tilde{p} = C_1 \frac{\sinh\sqrt{R^2 s/c}}{R} + C_2 \frac{\cosh\sqrt{R^2 s/c}}{R} - \frac{3\alpha}{S}\tilde{A}_1(s) \tag{73}$$

C_2 must still remain 0 so that the solution is bounded. We apply our new boundary conditions (Equation 3) and solve.

$$P_0 = C_1 \frac{\sinh\sqrt{R_0^2 s/c}}{R_0} - \frac{3\alpha}{S}\tilde{A}_1(s) \tag{74}$$

$$C_1 = \left(P_0 + \frac{3\alpha}{S}\tilde{A}_1(s)\right)\frac{R_0}{\sinh\sqrt{R_0^2 s/c}} \tag{75}$$

We can now substitute in our result for C_1 into Equation 73 to find that:

$$\tilde{p} = \frac{3\alpha}{S}\tilde{A}_1(s)\left(\frac{R_0\sinh\sqrt{R^2s/c}}{R\sinh\sqrt{R_0^2s/c}} - 1\right) + P_0\frac{R_0\sinh\sqrt{R^2s/c}}{R\sinh\sqrt{R_0^2s/c}} \tag{76}$$

As when deriving the solution for the previous loading mode we take the integrated solution for stress and apply our Laplace transform boundary conditions for stress and radius to find:

$$\tilde{\sigma}_{RR} = \left[-\frac{24\eta^2(1-v)}{S(1-2v)}\frac{R^*\sqrt{s^*}\cosh(R^*\sqrt{s^*}) - \sinh(R^*\sqrt{s^*})}{{R^*}^3 s^*\sinh\sqrt{s^*}}\right. \tag{77}$$

$$\left. + \frac{8\eta^2(1-v) + 2GS(1+v)}{S(1-2v)}\right]\tilde{A}_1(s) \tag{78}$$

$$0 = \left[-\frac{24\eta^2(1-v)}{S(1-2v)}\frac{\sqrt{s^*}\cosh\sqrt{s^*} - \sinh\sqrt{s^*}}{s^*\sinh\sqrt{s^*}}\right. \tag{79}$$

$$\left. + \frac{8\eta^2(1-v) + 2GS(1+v)}{S(1-2v)}\right]\tilde{A}_1(s) \tag{80}$$

$$\tilde{A}_1(s) = 0 \tag{81}$$

We can now eliminate $\tilde{A}_1(s)$ from our incomplete solution (Equation 76):

$$\frac{s\tilde{p}}{P_0} = \frac{R_0\sinh\sqrt{R^2s/c}}{R\sinh\sqrt{R_0^2s/c}} \tag{82}$$

Where the consolidation coefficient can be used to tidy up our result:

$$c = \frac{\kappa}{S} = \frac{\kappa G(v_u - v)}{2\eta^2(1-v)(1-v_u)} \tag{83}$$

And in the limiting case of incompressible constituents the consolidation coefficient reduces to:

$$c = \frac{\kappa G(1-v)}{(1-2v)} \tag{84}$$

We replace all variables with previously defined dimensionless alternatives:

$$\frac{\tilde{p}}{P_0} = \frac{\sinh\sqrt{{R^*}^2 s^*}}{sR^*\sinh\sqrt{s^*}} \tag{85}$$

Same as before we want to eliminate our hyperbolic functions using Equation 59:

$$\frac{\tilde{p}}{P_0} = \frac{\sin\sqrt{{R^*}^2 x_n}}{x_n R^*\sin\sqrt{x_n}} \tag{86}$$

Our Laplace transformed pore pressure solution can once again be expressed as the ratio of two analytic functions ($\tilde{f}_s = h(s)/g(s)$). We can use Equation 54 to return to the time domain as $g(s)$ once agin contains zeroes at $s_i, i = 1, 2...n$. In our case we find:

$$h(s) = \sin\sqrt{R^{*2} x_n} \tag{87}$$

and:

$$g(s) = x_n R^* \sin\sqrt{x_n} \tag{88}$$

where the derivative of $g(s)$ is:

$$g'(s) = R^* \sin\sqrt{x_n} + \frac{1}{2} R^* \sqrt{x_n} \cos\sqrt{x_n} \tag{89}$$

Ultimately this means we are able to solve for pressure using Equation 90:

$$\frac{p(R,t)}{P_0} = 1 + \sum_{n=1}^{\infty} \frac{\sin\sqrt{R^{*2} x_n}}{R^* \sin\sqrt{x_n} + \frac{1}{2} R^* \sqrt{x_n} \cosh\sqrt{x_n}} e^{-x_n t} \tag{90}$$

Where x_n is the roots of $g(s)$:

$$0 = x_n R^* \sin\sqrt{x_n} \tag{91}$$

7.2 Displacement

We recall our Laplace transformed solution for strain (Equation 65), knowing that under these boundary conditions $\tilde{A}_1 = \tilde{A}_2 = 0$:

$$\tilde{u}_R(R,s) = \frac{\eta}{G} \frac{1}{R^2} \int R^2 \tilde{p}(R,t) dR \tag{92}$$

Where $\tilde{p}$ is:

$$\tilde{p} = \frac{P_0 R_0 \sinh\sqrt{R^2 s/c}}{sR \sinh\sqrt{R_0^2 s/c}} \tag{93}$$

We solve the integration to find:

$$s\tilde{u}_R = \frac{3cnP_0 s \left[\sqrt{R^2 s/c} \cosh\sqrt{R^2 s/c} - \sinh\sqrt{R^2 s/c}\right]}{R^2 s \sinh\sqrt{R_0^2 s/c}} \tag{94}$$

Where we have tripled our solution to normalise it. We them make our equation dimensionless:

$$\frac{\tilde{u}_R}{u_R(R_0, \infty)} = \frac{3\left[\sqrt{R^{*2} s^*} \cosh\sqrt{R^{*2} s^*} - \sinh\sqrt{R^{*2} s^*}\right]}{R^{*2} s^{*2} \sinh\sqrt{s^*}} \tag{95}$$

Where now u_R becomes:

$$u_R(R_0, \infty) = \frac{\eta P_0 R_0}{G} \tag{96}$$

And:

$$\eta = \frac{\alpha(1-2v)}{2(1-v)} \tag{97}$$

We remove the complex component of the argument then apply our equation for the inverse Laplace transform (Equation 54) to find:

$$h(x_n) = 3\left[\sqrt{R^{*2}x_n}\cos\sqrt{R^{*2}x_n} - \sin\sqrt{R^{*2}x_n}\right] \tag{98}$$

and:

$$g(x_n) = R^{*2}{x_n}^2 \sin\sqrt{x_n} \tag{99}$$

where the derivative of $g(s)$ is:

$$g'(x_n) = \frac{1}{2}R^2 x_n(4\sin\sqrt{x_n} + \sqrt{x_n}\cos\sqrt{x_n}) \tag{100}$$

Ultimately this means that the analytical displacement solution under osmotic loading conditions is:

$$\frac{u_R}{u_R(R_0,\infty)} = R^* + \sum_{n=1}^{\infty} \frac{6\left[\sqrt{R^{*2}x_n}\cos\sqrt{R^{*2}x_n} - \sin\sqrt{R^{*2}x_n}\right]}{R^2 x_n(4\sin\sqrt{x_n} + \sqrt{x_n}\cos\sqrt{x_n})} e^{-x_n t} \tag{101}$$

7.3 Loading by Fluid Pressure

The solution under fluid pressure loading (mode 3) is merely a superposition of both previous loading modes. As such while not explicitly stated for brevity, the solution for pore pressure is the sum of Equation 63 and Equation 90, while the displacement solution is the sum of Equation 69 and Equation 101.

8 Results and Discussion

8.1 Numerical Inverse Laplace Transform

We have derived Laplace transformed solutions for pore pressure and displacement when loaded by direct stress or pore pressure (Equations 52, 69, 85 and 95) and have subsequently used the Cauchy residue theorem to convert these solutions to the time domain. For the purpose of validation we also choose to numerically invert our Laplace transformed solutions.

Abate and Whitt provide a comprehensive review of popular numerical methods for the inverse Laplace transform [54], based on this we opt to use Talbot's method [55] as it is 1.5 times more efficient that the Gaver-Stehfest one-dimensional algorithm and remains efficient under multiple use cases [54]. The MATLAB script for Talbot's method formulated under Abate and Whitt's unified framework [54] is provided by McClure [56].

As an example the MATLAB code for how to invert the complex frequency solution to pressure in Cryer's problem (Equation 52) is shown below:

Listing 1: MATLAB code for the numerical inverse Laplace transform for the pressure solution of Cryer's problem using Talbot's method.

```
i = 1;
n = 100;    %the number of radial steps
for t=[0.001,0.01,0.1,0.2,0.3,1]    %dimensionless times (t*)
        i=i+1;
        for j=0:1:n    %evaluate along length of the radius
                R=j/n;    %calculate dimensionless radius (R*)
                f_s = @(s) (s*(sinh(R*sqrt(s))-R*sinh(sqrt(s))))/(s*R*(4*n*sqrt(s)*cosh(sqrt(s))-(s+4*n)*sinh(sqrt(s))));
                cryer(j+1,i) = talbot_inversion(f_s, t);    %Talbot's method script
        end
end
```

8.2 Analytical Inverse Laplace Transform

A root finding algorithm written in MATLAB based on the bisection method is used to find the roots of $g(s)$ (Equations 64 and 91) [57]. The algorithm finds roots by detecting local sign changes within a restricted range of the whole function (within a window):

Listing 2: MATLAB root finder.

```
g_s = @(x) -x*sin(sqrt(-x)); % the function g(s)
b=10;    %the window size. Larger numbers are faster but some roots may be skipped.
b_max=10000;    %search for roots up until b_max. This is a truncation of an infinite series, larger numbers are more accurate but take longer.
for lb=0:b:b_max %lb=lower bound of window for algorithm
        ub=lb+b; %ub=upper bound of window for algorithm
        all_roots(lb/b+1)=bisection(g_s,lb,ub);
end
```

This simple code is sufficient in finding the roots of $g(s)$ under osmotic boundary conditions. The function, and the identified roots, are plotted in Figure 2.

The bisection method (and most root finding algorithms) search for roots in a function by checking for a sign inversion in the output of the function [58]. However, sign inversions do not just occur about roots, they also occur in asymptotic functions. To help

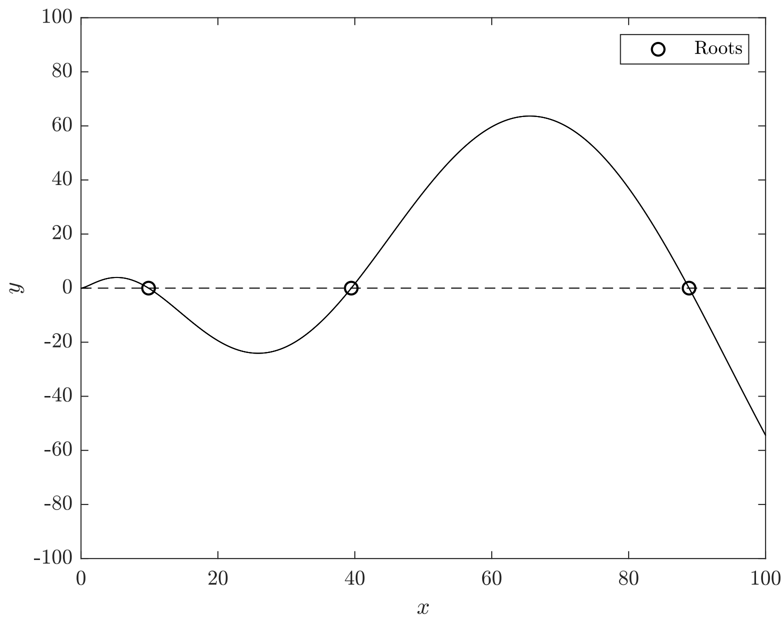

Figure 2: Roots of the function $g(s)$ under osmotic loading boundary conditions (Equation 91). The standard bisection MATLAB root finder is sufficient.

visualise this we plot $g(s)$ as derived from Cryer's problem (Equation 64 in Figure 3).

As mentioned in Figure 3 the MATLAB script erroneously detects asymptotes as roots. We modify our script to extract only the roots, ignoring the sign inversions occurring at asymptotes. We do this by looping through a vector of all roots (true and false), checking that the result of the function $g(s) \approx 0$ while the asymptotic false roots by definition tend to infinity.

Listing 3: Corrected MATLAB root finder.

```
v=0.25;    %poisson's ratio
g_s = @(x) (2*(1-2*v)*sqrt(x))/(2*(1-2*v)-(1-v)*x)-tan(sqrt(x));
b=10;
b_max=10000;
for lb=0:b:b_max
        ub=lb+b;
        all_roots(lb/b+1)=bisection(g_s,lb,ub);
        x=all_roots(lb/b+1);
        if -1<(2*(1-2*0.25)*sqrt(x))/(2*(1-2*0.25)-(1-0.25)*x)-
            tan(sqrt(x)) && (2*(1-2*0.25)*sqrt(x))/(2*(1-2*0.25)
            -(1-0.25)*x)-tan(sqrt(x))<1    %check if -1 < g(s) < 1
                true_roots(lb/b+1)=x;
        else
```

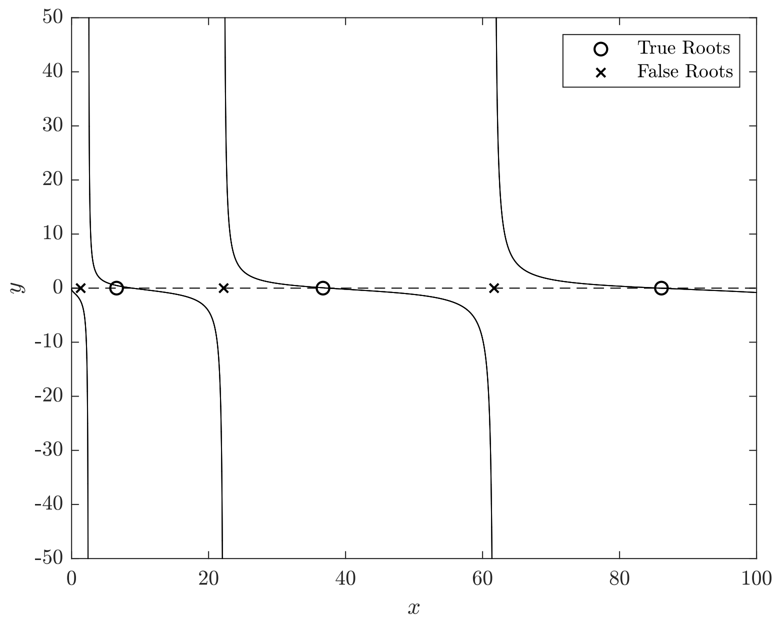

Figure 3: The function $y = \frac{2(1-2v)\sqrt{x}}{2(1-2v)-(1-v)x_n} - \tan\sqrt{x}$ (Equation 64). We use the bisection method to identify the roots. Some roots are correctly identified (**o**), while others are incorrectly identified occurring at asymptotes (**x**).

```
                false_roots(lb/b+1)=x;
            end
        end
```

After finding the correct roots it is trivial to solve our pressure solution (Equation 63).

Listing 4: MATLAB.

```
        i = 1;
        n = 100;    %the number of radial steps
        for t=[0.001,0.01,0.1,0.2,0.3,1]    %dimensionless times (t*)
            i=i+1;
                for j=0:1:n    %evaluate along length of the radius
                R=j/n;    %calculate dimensionless radius (R*)
                for k=1:length(true_roots)    %loop through every root
                    cryer_sum(k)=(4*(1-v)*(1-2*v)*(sin(R*sqrt(true_roots(k)))-R*sin(sqrt(true_roots(k)))))/(((1-v)^2*true_roots(k)-2*(1+v)*(1-2*v))*R*sin(sqrt(true_roots(k))))*exp(-true_roots
```

```
                              (k)*t);
                    end
                    cryer_pressure(j+1,i)=sum(cryer_sum);    %
                       summation
             end
      end
```

8.3 Finite Element Simulation

As one final form of validation, a computational simulation of Cryer's problem was created in ABAQUS. Unfortunately, a simulation of the second loading mode was unable to be prepared as ABAQUS does not allow for a stress of zero to be applied on the solid skeleton.

An axisymmetric model of a spherical ball was created and meshed using CAX4P linear elements. Material parameters used for this simulation are not stated in this report as ultimately all results were made dimensionless using the previously defined values for R^* and t^* (see Equations 47 and 58).

Boundary value problems for which loading is instantaneous often have large gradients at the instant of loading, and as such require particularly fine time stepping about this point. The optimum value for this time step, Δt, has been derived by Vermeer and Verruijt [59]:

$$\Delta t \geq \frac{\gamma_w}{6E\kappa}(\Delta h)^2 \tag{102}$$

Where γ_w is the specific weight of the interstitial fluid, E is the Young's modulus of the poroelastic material, κ is permeability and Δh is the element size at this boundary, determined with a convergence analysis as show below. Using this relationship we find the appropriate time stepping for the transient soil analysis.

Mesh convergence was determined by plotting the peak pore pressure recorded in the sphere when $R = 0$ and $\nu = 0.25$. Cryer's analytical solution for pore pressure, Equation 63, predicts a pore increase of just over 1.3 times the applied load due to the Mandel-Cryer effect. This effect will be discussed later in the report, for now note from Figure 4 how as the number of elements increase the computational value approaches the analytical value. Although convergence is reached around 500 elements, all simulations in this report were preformed at 1000 elements.

8.4 Pore Pressure

We begin by plotting Cryer's solution for pore pressure as a function of radius and time with the assumption of incompressible constituents where $\nu = 0.25$ (Equation 63). As previously mentioned this is a well established result originally derived in 1963 [37].

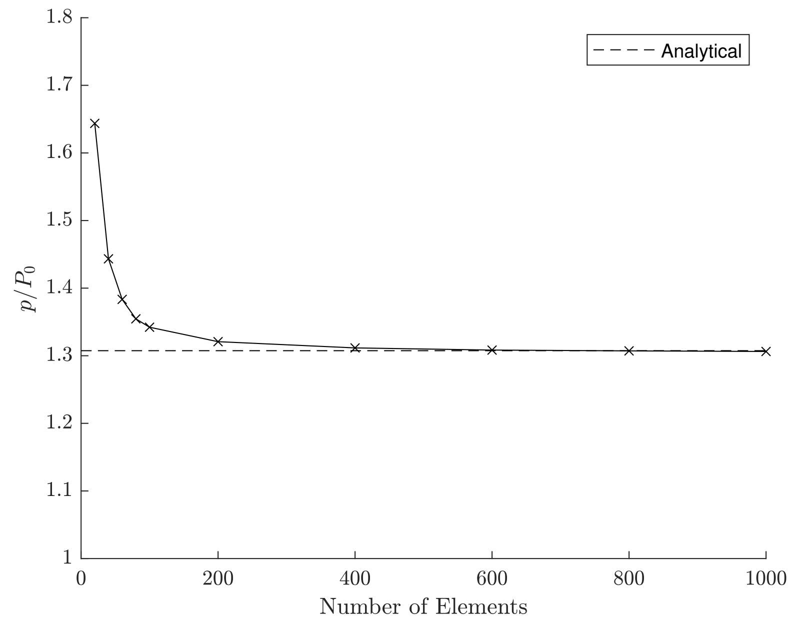

Figure 4: Peak pressure at the centre of a poroelastic sphere undergoing consolidation through direct stress loading as simulated with ABAQUS. The pressure peaks above the applied load due to the Mandel-Cryer effect. Consolidation of the computational and analytical pore pressure is reached around 500 elements, although all future ABAQUS simulations are run using 1000 elements.

Although not the objective of this thesis, we plot Cryer's solution to validate our chosen numerical method of finding the inverse of Laplace transformed functions (Talbot's method [55]), our converged ABAQUS simulation and the underlying analytical MATLAB code itself.

From Figure 5 we can clearly observe that the analytical, numerical and computational results are all in good agreement. Note however that Talbot's numerical Laplace inversion begins to become unstable for smaller times (e.g. when $t^* = 0.001$), leading to a small perturbation in the expected results. The unconditional stability of most numerical methods is one reason why analytical solutions are often preferred.

Figure 5 also shows that pore pressure is expected to rise above the applied load, particularly near the centre of the sphere - this is due to the Mandel-Cryer effect. To better visualise this phenomenon, in Figure 6 pore pressure at the centre of the sphere is plotted a function of time.

The Mandel-Cryer effect can be explained by considering fluid drainage from the poroelastic skeleton. The instant we start loading the sphere the pore pressure is equal in

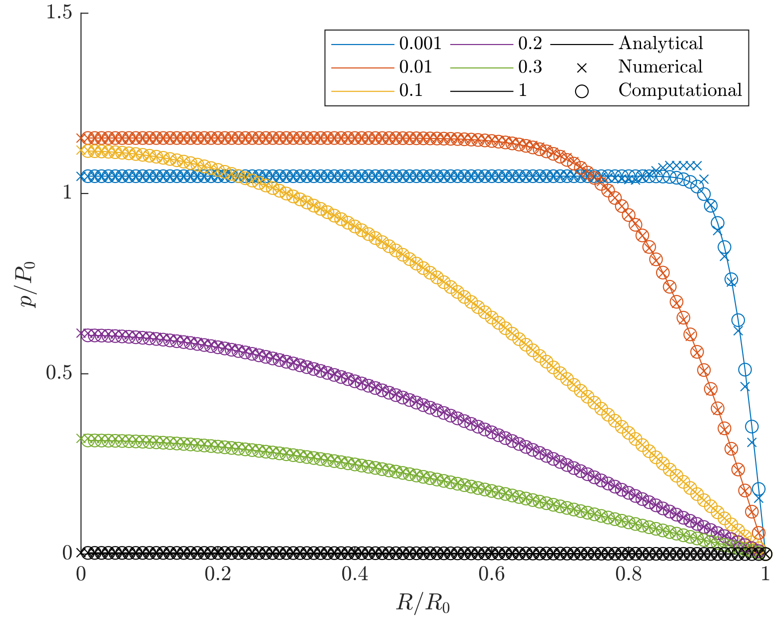

Figure 5: Pore pressure in a consolidating sphere as a function of radius and time under Cryer's boundary conditions where $\nu = 0.25$. There is good agreement between analytical, numerical and computational results, although there is some slight instability using the numerical inverse Laplace transform for small values of dimensionless time.

magnitude to the applied stress (recall from Cryer's boundary conditions that $-\sigma_{RR} = P_0 H(t-0)$). However, at $p = 0$ as $R = R_0$ the fluid is able to freely drain from the surface of the consolidating sphere. This dissipation in pore pressure means that shortly after loading, the sphere effectively becomes an inhomogeneous material, with a more compliant draining outer shell and a stiffer non-draining core [43]. This causes stress to distribute non-uniformly along the radius of the consolidating sphere, causing a comparatively higher pore pressure at the centre of the sphere. The pore pressure will eventually dissipate as $t^* \to 1$, which is also demonstrated in Figure 6.

Note also that the Mandel-Cryer effect is more pronounced as $\nu \to 0$. This is because Poisson's ratio is the ratio of transverse strain to axial strain. This means that for lower values of ν there is more stain radially than there is tangentially. From Hooke's law we know that stress is proportional to stain [60], therefore we know that lower Poisson's ratios must result in more radial stress, consequently increasing the severity of the Mandel-Cryer effect. This relationship has even been found to be even more severe for materials with negative Poisson's ratios [61].

Having verified that our three separate methods of simulating poroelastic consolidation are valid for Cryer's boundary conditions we move to plotting our derived pore

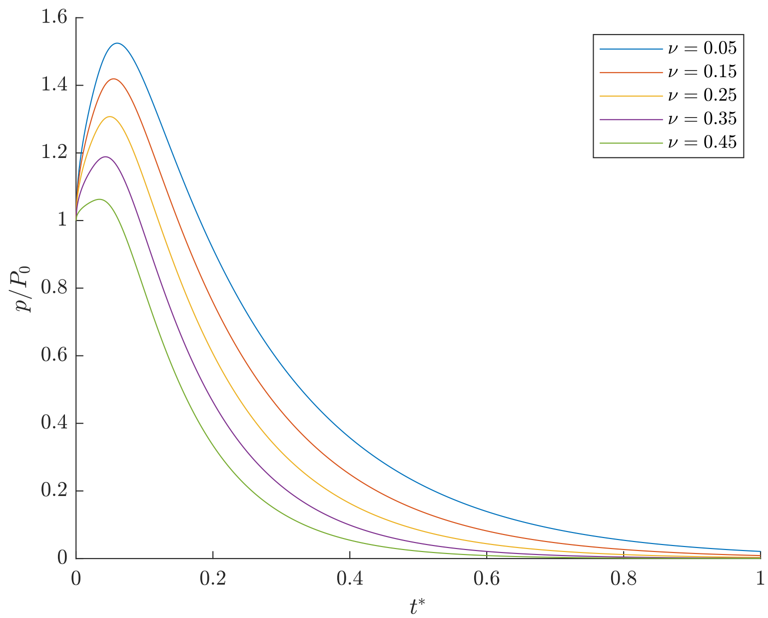

Figure 6: Pore pressure at the centre of a consolidating sphere subjected to Cryer's boundary conditions. The pore pressure peaks above the applied stress due to the Mandel-Cryer effect, with effect being more severe as $\nu \to 0$. The Mandel-Cryer effect occurs due to fluid drainage at the surface of the sphere creating a more compliant material, resulting in increased loading on the relatively stiffer core.

pressure solution under osmotic boundary conditions (Equation 85 in the complex frequency domain and Equation 90 in the time domain).

Unfortunately, as previously mentioned, ABAQUS is unable to simulate this loading mode as stress cannot be set to a value of zero. Nevertheless Figure 7 demonstrates a good agreement between analytical and numerical results.

From Figure 7 it is immediately obvious that there is no Mandel-Cryer effect under these boundary conditions. This is expected, the Mandel-Cryer effect occurs due to drainage at the surface of the sphere, but now that $p = P_0 H(t-0)$ drainage is unable to occur. Instead as $t^* \to 1$ the pore pressure across the entire sphere equalises at P_0.

This solution is actually nearly identical to the diffusion equation, an observation that can be easily verified by looking back at our pressure solution before the Laplace transform (Equation 35). With the benefit of hindsight we know that $A_1 = 0$, eliminating the right hand side of the equation entirely and leaving only the diffusion equation, with the consolidation coefficient replacing diffusivity.

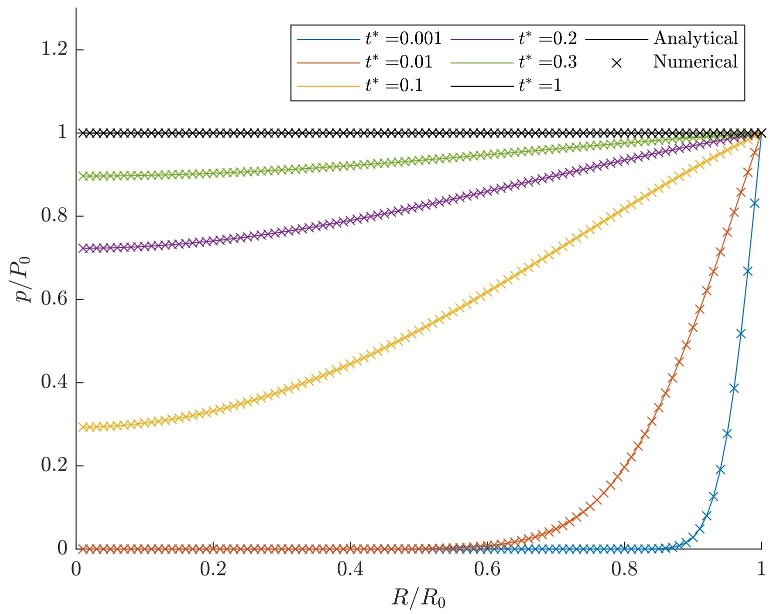

Figure 7: Pore pressure in a consolidating sphere as a function of radius and time under osmotic boundary conditions. There is no dependence on Poisson's ratio. This results is identical to the solution to the diffusion equation.

Viewed this way the solution of pore pressure under mode 2 loading can be described by thinking of pore pressure as analogous to a concentrated solute, diffusing down a concentration gradient into the sphere, gradually raising the pressure inside until equilibrium is achieved.

As one final observation from Figure 7 note that under this loading mode the result is not dependent on Poisson's ratio, which is confirmed by looking at Equation 90. This result is expected, Poisons ratio is irrelevant as we are not concerned with stress being loaded on the solid skeleton and the fluid is assumed to be incompressible.

We continue as before by plotting the pore pressure at the centre of the sphere as a function of time (see Figure 8). Unlike Cryer's result in which the pore pressure change is instantaneous, the osmotic loading condition has a slight lag before any pore pressure change is observed at the centre of the sphere. This phenomenon can be understood by returning to the diffusion analogy - time is required before the diffusing pore pressure can reach the centre and cause an increase in pore pressure.

As previously mentioned, the final loading mode (that of loading through applied fluid pressure) is the superposition of both previous loading modes. This result is plotted in Figure 9.

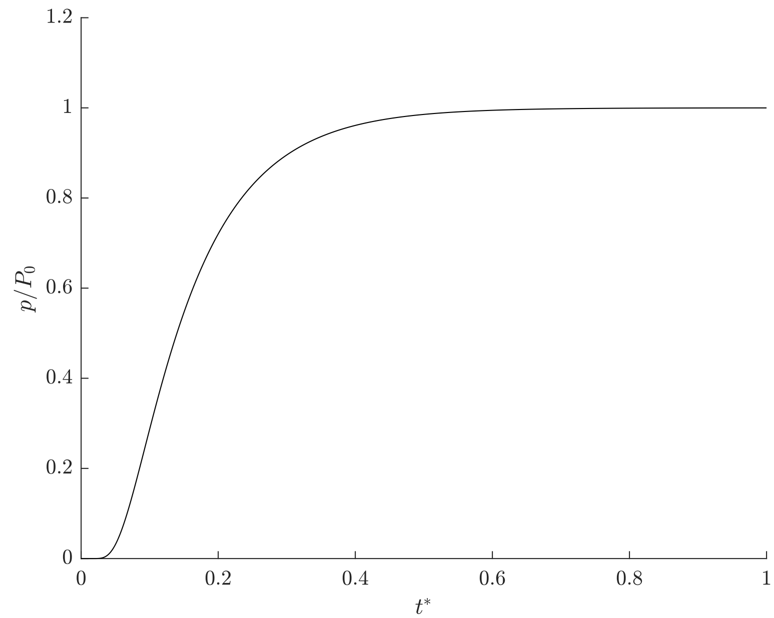

Figure 8: Pore pressure at the centre of a consolidating sphere subjected to osmotic boundary conditions.

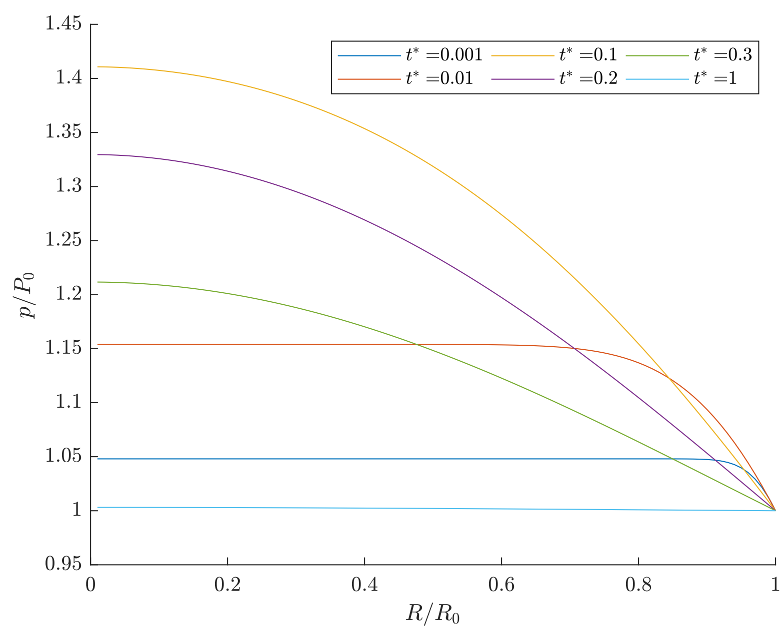

Figure 9: Analytical solution of pore pressure at the center of a consolidating sphere subjected to fluid pressure loading boundary conditions with $\nu = 0.25$.

At both the instant of loading and when $t^* = 1$ pressure across the radius of the sphere is equal to P_0. The increase and subsequent decrease in pore pressure at the centre of the sphere is most likely due to stress applied directly on the solid skeleton being transferred to the surrounding fluid. This higher pressure fluid now needs time to diffuse outwards and equalize, this process is slowest at the centre of the sphere where diffusion distances are greatest.

8.5 Displacement

Understanding how a consolidating sphere deforms as a function of time is critical in formulating an alternative to AFM. As previously mentioned the surface settlement of a cell in an osmotic medium can be fit against the previously derived governing equation to calculate certain mechanical properties. In this section a positive displacement is treated as the sphere expanding outwards while conversely a negative displacement is the sphere contracting.

We begin by plotting Cryer's solution for displacement with incompressible constituents and $\nu = 0.25$ in Figure 10. Notice immediately that our numerical and computational solutions match Cryer's analytical solution, validating our method.

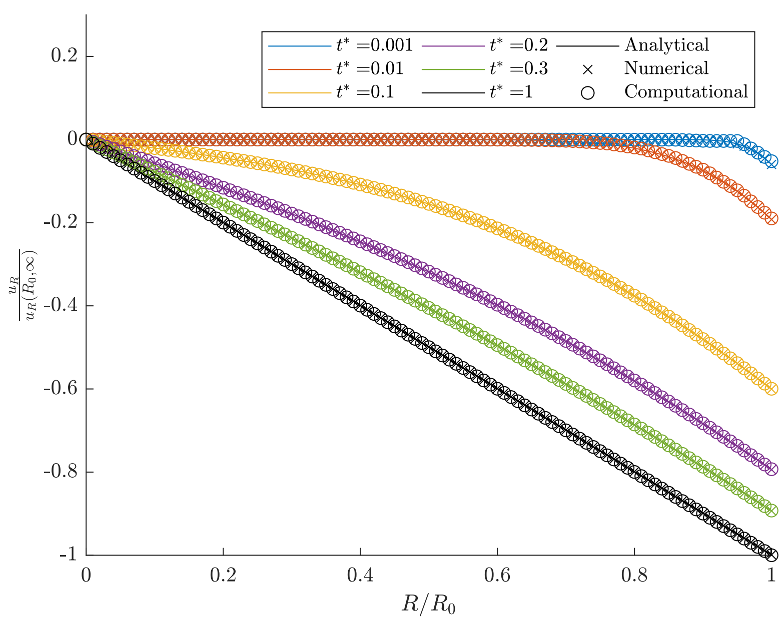

Figure 10: Displacement in a consolidating sphere loaded with Cryer's boundary condtitions with $\nu = 0.25$.

Displacements in Cryer's mode are all negative. Intuitively this is correct, strain is applied directly to the solid skeleton of the poroelastic sphere and when a linear elastic solid is loaded we expect it to compress.

Displacement itself is fixed at zero as defined by Cryer's boundary condition that $u_R = 0$ at $R = 0$. Displacement is highest at the surface of the sphere directly where the load is applied. In fact, when $t^* = 1$ there is an exact linear relationship between displacement and radial distance.

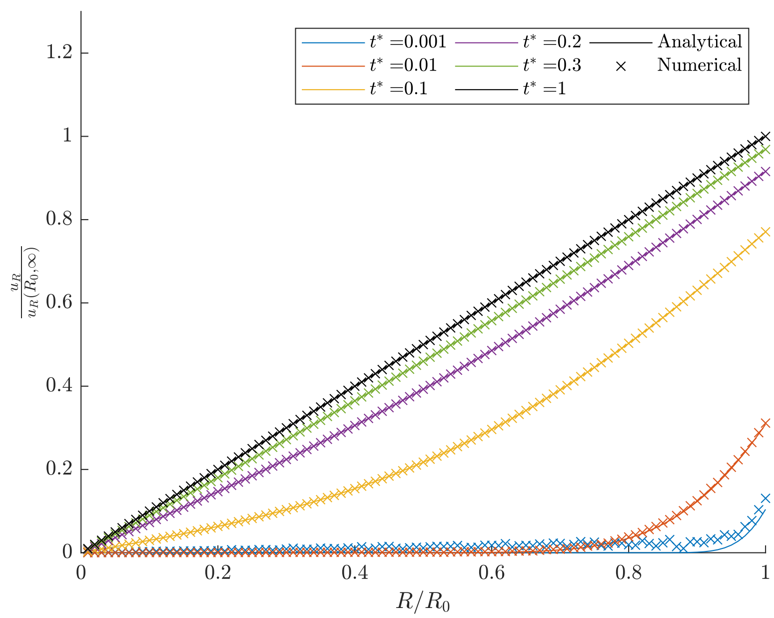

Figure 11: Displacement in a consolidating sphere under Mode 2 loading conditions.

When we plot displacement as a function of time and radius for the osmotic loading condition we now notice that the poroelastic sphere begins swelling (see Figure 11). This may seem unintuitive at first until you consider that under this mode loading is applied as pore pressure, which diffuses in and acts internally, pushing outwards on the solid skeleton.

Notice from Figure 11 that our results almost mirrors Figure 10 reflected in the x-axis - this means that a superposition of both loading modes results in no deformation. This initially confusing result is explained as follows. As we have made the assumption of incompressible constituents the soil does not immediately deform upon compression, and instead a pore pressure rise proportional to the applied stress will be produced based on the Skempton effect. This pore pressure rise acts in opposition to the applied pressure on the surface, cancelling it out and resulting in no net deformation.

The Skempton effect describes how the pore pressure in a poroelastic material increases (Δp) when said material is subjected to a compressive stress (ΔP) [43]:

$$\Delta p = B\Delta P \tag{103}$$

Where B is the Skempton pore pressure coefficient. Typically $0 \leq B \leq 1$ although $B > 1$ is also possible [43]. However under the assumption of incompressible constituents all load must be transferred into pore pressure and so $B = 1$.

The assumption of incompressible constituents is made frequently in poroelasticity, Cryer's original work made this assumption [37], as do Mason [41] and Nowinski and Davis [42]. In geomechanical analysis this assumption is often safe to make, however for cellular modelling the assumption is more tenuous. For example, it is safe to model cytosol as an incompressible Newtonian fluid [62], however there is no evidence proving it appropriate to model the solid skeleton of a cell in the same way. Nevertheless this assumption was made to reduce the number of mechanical parameters needed to characterise a cell. A larger number of parameters in the governing equation requires an higher degree polynomial to be used for curve fitting, which could lead to good fits that may still result in incorrectly determined parameters. Ideally any method of stiffness quantification should determine only a limited number of parameters. Unfortunately without more poroelastic cellular data available it is impossible to determine whether this assumption is safe to make.

Moving on, internal pressure and deformation of a consolidating cell is difficult to observe, however surface settlement of a swelling or shrinking cell can be easily captured with any microscope. As such we plot the surface deformation of a sphere swelling due to an osmotic pressure in Figure 12.

Surface deformation data can be matched against this function using curve fitting algorithms to calculate the cell's mechanical properties that ultimately define surface consolidation under osmotic loading - namely Poisson's ratio, shear modulus and permeability. Experimentally derived conversions exist for calculating the elastic modulus, bulk modulus and other parameters from these values if desired.

At present the reliance on permeability severely limits the viability of poroelastically modelling cells. Permeability data of various biological cells is thoroughly lacking and greater questions about the permeability of cells remains unanswered. Does permeability vary greatly on a cell by cell basis or can an assumed value be safely used? Is permeability homogeneous or inhomogeneous across the cell? Does the presence of certain organells significantly affect accurate measurements? A greater body of research on cell permeability is needed to answer these questions, to this end a streamlined way of accurately measuring cell permeability is required.

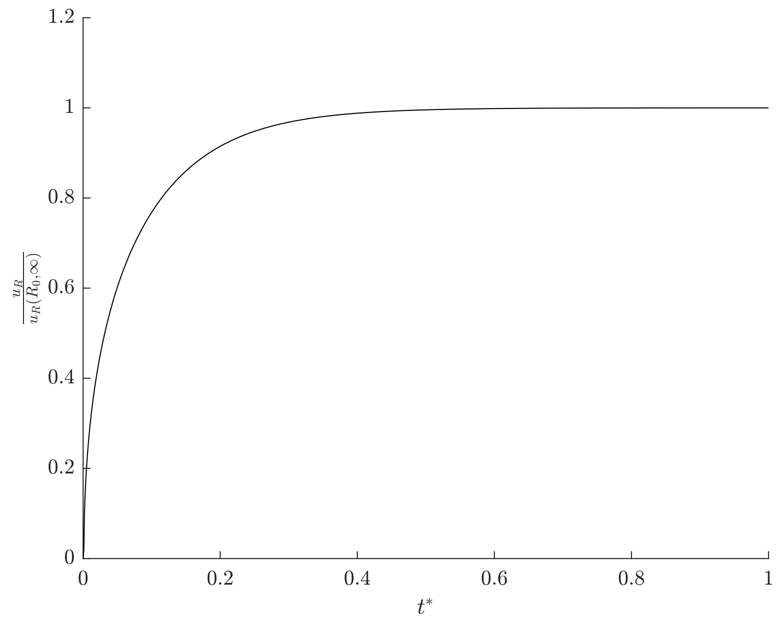

Figure 12: Displacement at the surface of a consolidating sphere loaded with osmotic boundary conditions.

Biot and Willis propose a few ways in which permeability (and other poroelastic coefficients) can be measured [63]. Unfortunately, methods such as the jacketed and unjacketed compression test are unsuited to micron sized cells. Instead two alternative techniques for determining permeability are presented:

Darcy's law is an equation relating flow rate through a permeable medium (Q) to permeability. Through a chamber of cross sectional area A there flows a fluid with viscosity μ. As there is a pressure drop ΔP over its length L we find permeability equal to [64]:

$$\kappa = -\frac{Q\mu L}{A\Delta P} \tag{104}$$

Despite originally being formulated in 1856 [65] Darcy's law is still regularly used to determine the permeability of rocks [66], fibre reinforced composites [67], bone [68] and even tissue engineered scaffolds [69].

Although the apparatus needed to measure permeability using Darcy's law is simple it requires a bulk quantity of poroelastic material to work - the volume of the testing chamber must be packed with cells. Producing such a large quantity of cells would be challenging, and even though the dimensions of the chamber can be scaled down to micron size that cells themselves may deform under the fluid flow.

Furthermore the membrane of the cells may impart some resistance on the flux of water, causing the streamlines to preferentially pass around the cells rather that through them as desired when measuring the permeability of the cytoplasm.

An alternative method of measuring permeability may be adapted from the work of Chan *et al.* [70]. Their method, called "Poroelastic Relaxation Indentation", is used to assess the permeability of micron scale hydrogels through indentation to a fixed depth. The load relaxation of the hydrogel is then recorded and used to determine various mechanical properties.

The finite element solution of the equation governing "Poroelastic Relaxation Indentation" [71] has successfully been used by Moeendarbary *et al.* to characterise the poroelastic properties of MDCK, HeLa and HT1080 cells [34], proving the feasibility of such a technique.

Unfortunately such a method is reliant on micro-indentation, and as such has the exact same limitations as AFM which motivated this report. However it may be necessary to use such techniques just to achieve a reference value for permeability, following on from which the osmotic deformation method presented in this report may be used.

9 Conclusion

While AFM remains the most effective way to assess local variances in stiffness within an inhomogenous tissue, often bulk assessment of cellular stiffness is desired. This thesis outlined six key criteria for any possible alternative to AFM, which we restate with evidence that the proposed method has achieved each criterion. The method must:

1. **be capable of quantifying cellular mechanical properties** - an equation describing cell swelling or shrinkage as determined by shear modulus, Poisson's ratio and permeability has been derived.

2. **require equipment typically found in most labs** - only a microscope, trypsin and a hypoosmotic or hyperosmotic solution is required.

3. **be quick** - the speed of water flux across the cell membrane can be controlled by changing the osmotic pressure.

4. **assess several cells in tandem** - multiple swelling cells can be viewed and measured under the same microscope using existing software capable of cell tracking (e.g. ImageJ).

5. **not damage the cell** - although *in vitro* verification is needed, the process is entirely reversible unless the threshold for osmotic shock is exceeded.

6. **not allow for cell adhesion** - the cell has been trypsinized, preventing integrin binding.

Although the derived analytical solution has been validated using numerical methods and computational simulations, experimental validation has not been achieved. It is entirely possible that the proposed method may not be a viable way to determine cellular stiffness. A series of question must be answered before the viability of the method is ensured:

- Are trypsinised cells sufficiently spherical?
- Aquaporins are integral membrane proteins embedded in cellular membranes that facilitate the transport of water [72]. Do they significantly effect the predicted flux of water?
- A cell has been modelled as a singular poroelastic domain with the phospholipid bilayer being a dimensionless partially permeable membrane. Does the solution need to be expanded to a two layer problem with the membrane being mechanically characterised independently?
- Does the membrane itself sufficiently impede the passage of water?
- Most obviously, does the predicted stiffness match recorded values for cellular stiffness?

Should these questions be answered through rigours experimental validation, the proposed method for quantifying cellular stiffness may offer a simple, low-cost alternative to AFM.

Mechanotransduction itself is a nascent field of research that forms an essential part of cellular biology. Unfortunately many cellular biologists have not had the opportunity to consistently probe cellular stiffness due to the prohibitive cost of AFM and other technologies. This method will ultimately never replace AFM, but if experimentally validated, it may offer a reliable - and very accessible - alternative.

References

[1] Peter Fratzl and Richard Weinkamer. Nature's hierarchical materials. *Progress in materials Science*, 52(8):1263–1334, 2007.

[2] Donald Ingber. Mechanobiology and diseases of mechanotransduction. *Annals of medicine*, 35(8):564–577, 2003.

[3] Surya M Nauli, Francis J Alenghat, Ying Luo, Eric Williams, Peter Vassilev, Xiaogang Li, Andrew EH Elia, Weining Lu, Edward M Brown, Stephen J Quinn, et al. Polycystins 1 and 2 mediate mechanosensation in the primary cilium of kidney cells. *Nature genetics*, 33(2):129, 2003.

[4] Florence Broders-Bondon, Thanh Huong Nguyen Ho-Bouldoires, Maria-Elena Fernandez-Sanchez, and Emmanuel Farge. Mechanotransduction in tumor progression: the dark side of the force. *J Cell Biol*, 217(5):1571–1587, 2018.

[5] Diana E Jaalouk and Jan Lammerding. Mechanotransduction gone awry. *Nature reviews Molecular cell biology*, 10(1):63, 2009.

[6] Gerd K Bennig. Atomic force microscope and method for imaging surfaces with atomic resolution, February 9 1988. US Patent 4,724,318.

[7] Kristina Haase and Andrew E Pelling. Investigating cell mechanics with atomic force microscopy. *Journal of The Royal Society Interface*, 12(104):20140970, 2015.

[8] Daniel Rugar and Paul Hansma. Atomic force microscopy. *Physics today*, 43(10):23–30, 1990.

[9] Victor J Morris, Andrew R Kirby, and A Patrick Gunning. *Atomic force microscopy for biologists*. World Scientific, 1999.

[10] M Radmacher, RW Tillamnn, M Fritz, and HE Gaub. From molecules to cells: imaging soft samples with the atomic force microscope. *Science*, 257(5078):1900–1905, 1992.

[11] Tatyana G Kuznetsova, Maria N Starodubtseva, Nicolai I Yegorenkov, Sergey A Chizhik, and Renat I Zhdanov. Atomic force microscopy probing of cell elasticity. *Micron*, 38(8):824–833, 2007.

[12] Heinrich Rudolf Hertz. Uber die beruhrung fester elastischer korper und uber die harte. *Verhandlung des Vereins zur Beforderung des GewerbefleiBes, Berlin*, page 449, 1882.

[13] Ian N Sneddon. The relation between load and penetration in the axisymmetric boussinesq problem for a punch of arbitrary profile. *International journal of engineering science*, 3(1):47–57, 1965.

[14] RE Mahaffy, CK Shih, FC MacKintosh, and J Käs. Scanning probe-based frequency-dependent microrheology of polymer gels and biological cells. *Physical review letters*, 85(4):880, 2000.

[15] Anja Vinckier and Giorgio Semenza. Measuring elasticity of biological materials by atomic force microscopy. *FEBS letters*, 430(1-2):12–16, 1998.

[16] H-J Butt, P Siedle, K Seifert, K Fendler, T Seeger, E Bamberg, AL Weisenhorn, K Goldie, and A Engel. Scan speed limit in atomic force microscopy. *Journal of microscopy*, 169(1):75–84, 1993.

[17] Toshio Ando, Noriyuki Kodera, Eisuke Takai, Daisuke Maruyama, Kiwamu Saito,

and Akitoshi Toda. A high-speed atomic force microscope for studying biological macromolecules. *Proceedings of the National Academy of Sciences*, 98(22):12468–12472, 2001.

[18] ADL Humphris, MJ Miles, and JK Hobbs. A mechanical microscope: High-speed atomic force microscopy. *Applied physics letters*, 86(3):034106, 2005.

[19] LM Picco, L Bozec, A Ulcinas, DJ Engledew, M Antognozzi, MA Horton, and MJ Miles. Breaking the speed limit with atomic force microscopy. *Nanotechnology*, 18(4):044030, 2006.

[20] Toshio Ando. High-speed atomic force microscopy coming of age. *Nanotechnology*, 23(6):062001, 2012.

[21] SC Minne, SR Manalis, and CF Quate. Parallel atomic force microscopy using cantilevers with integrated piezoresistive sensors and integrated piezoelectric actuators. *Applied Physics Letters*, 67(26):3918–3920, 1995.

[22] SC Minne, G Yaralioglu, SR Manalis, JD Adams, J Zesch, Abdullah Atalar, and CF Quate. Automated parallel high-speed atomic force microscopy. *Applied Physics Letters*, 72(18):2340–2342, 1998.

[23] Christopher S Chen. Mechanotransduction–a field pulling together? *Journal of cell science*, 121(20):3285–3292, 2008.

[24] Keir C Neuman and Attila Nagy. Single-molecule force spectroscopy: optical tweezers, magnetic tweezers and atomic force microscopy. *Nature methods*, 5(6):491, 2008.

[25] Ming Dao, Chwee Teck Lim, and Subra Suresh. Mechanics of the human red blood cell deformed by optical tweezers. *Journal of the Mechanics and Physics of Solids*, 51(11-12):2259–2280, 2003.

[26] Arthur Ashkin, James M Dziedzic, JE Bjorkholm, and Steven Chu. Observation of a single-beam gradient force optical trap for dielectric particles. *Optics letters*, 11(5):288–290, 1986.

[27] JP Mills, L Qie, M Dao, CT Lim, S Suresh, et al. Nonlinear elastic and viscoelastic deformation of the human red blood cell with optical tweezers. 2004.

[28] Y Liu, DK Cheng, GJ Sonek, MW Berns, CF Chapman, and BJ Tromberg. Evidence for localized cell heating induced by infrared optical tweezers. *Biophysical journal*, 68(5):2137–2144, 1995.

[29] Steven P Gross. [8] application of optical trapsin vivo. In *Methods in enzymology*, volume 361, pages 162–174. Elsevier, 2003.

[30] Raymond HW Lam, Shinuo Weng, Wei Lu, and Jianping Fu. Live-cell subcellular measurement of cell stiffness using a microengineered stretchable micropost array membrane. *Integrative Biology*, 4(10):1289–1298, 2012.

[31] Yang Liu, Rebecca Medda, Zheng Liu, Kornelia Galior, Kevin Yehl, Joachim P Spatz, Elisabetta Ada Cavalcanti-Adam, and Khalid Salaita. Nanoparticle tension probes patterned at the nanoscale: impact of integrin clustering on force transmission. *Nano letters*, 14(10):5539–5546, 2014.

[32] CS Simmons, JY Sim, P Baechtold, A Gonzalez, C Chung, N Borghi, and BL Pruitt. Integrated strain array for cellular mechanobiology studies. *Journal of Micromechanics and Microengineering*, 21(5):054016, 2011.

[33] H Dalen and PW Todd. Surface morphology of trypsinized human cells in vitro. *Experimental cell research*, 66(2):353–361, 1971.

[34] Emad Moeendarbary, Léo Valon, Marco Fritzsche, Andrew R Harris, Dale A Moulding, Adrian J Thrasher, Eleanor Stride, L Mahadevan, and Guillaume T Charras. The cytoplasm of living cells behaves as a poroelastic material. *Nature materials*, 12(3):253, 2013.

[35] Larry Taber, Yunfei Shi, Le Yang, and Philip Bayly. A poroelastic model for cell crawling including mechanical coupling between cytoskeletal contraction and actin polymerization. *Journal of mechanics of materials and structures*, 6(1):569–589, 2011.

[36] Trung Dung Nguyen, Adekunle Oloyede, and Yuantong Gu. Stress relaxation analysis of single chondrocytes using porohyperelastic model based on afm experiments. *Theoretical and Applied Mechanics Letters*, 4(5):054001, 2014.

[37] CWA Cryer. A comparison of the three-dimensional consolidation theories of biot and terzaghi. *The Quarterly Journal of Mechanics and Applied Mathematics*, 16(4):401–412, 1963.

[38] CRI Clayton, H Müller Steinhagen, and W Powrie. Terzaghi's theory of consolidation, and the discovery of effective stress. In *Proceedings of the Institution of Civil Engineers: Geotechnical Engineering*, volume 113, 1995.

[39] RE Gibson. Some aspects of one-dimensional consolidation and contaminant transport in wastes. *Compression and consolidation of clayey soils*, pages 815–832, 1995.

[40] Cheikhou Ndiaye, Meissa Fall, Mapathe Ndiaye, Daouda Sangare, and Abib Tall. A review and update of analytical and numerical solutions of the terzaghi one-dimensional consolidation equation. *Open Journal of civil engineering*, 4(03):274, 2014.

[41] DP Mason, A Solomon, and LO Nicolaysen. Evolution of stress and strain during the consolidation of a fluid-saturated porous elastic sphere. *Journal of applied physics*, 70(9):4724–4740, 1991.

[42] JL Nowinski and CF Davis. A model of the human skull as a poroelastic spherical shell subjected to a quasistatic load. *Mathematical Biosciences*, 8(3-4):397–416, 1970.

[43] Alexander H-D Cheng. *Poroelasticity*. Springer, 2016.

[44] Arnold Verruijt. *An Introduction to Soil Mechanics*, volume 30. Springer, 2017.

[45] Md Tauhidul Islam and Raffaella Righetti. An analytical poroelastic model of a spherical tumor embedded in normal tissue under creep compression. *Journal of biomechanics*, 89:48–56, 2019.

[46] Amin Mehrabian and Younane N Abousleiman. Theory and analytical solution to cryer's problem of n-porosity and n-permeability poroelasticity. *Journal of the Mechanics and Physics of Solids*, 118:218–227, 2018.

[47] RE Gibson, A Gorbeth, and RL Schiffman. On cryer's problem with large displacements and variable permeability. *Géotechnique*, 40(4), 1990.

[48] Nicholas P Money. Osmotic pressure of aqueous polyethylene glycols: relationship between molecular weight and vapor pressure deficit. *Plant physiology*, 91(2):766–769, 1989.

[49] Christopher B Stanley and Helmut H Strey. Measuring osmotic pressure of poly (ethylene glycol) solutions by sedimentation equilibrium ultracentrifugation. *Macromolecules*, 36(18):6888–6893, 2003.

[50] Phillip L Gould and Yuan Feng. *Introduction to linear elasticity*. Springer, 1994.

[51] William S Slaughter. *The linearized theory of elasticity*. Springer Science & Business Media, 2012.

[52] Andi hani. An introduction to linear poroelasticity. *arXiv preprint arXiv:1607.04274*, 2016.

[53] Peter D Lax and Robert D Richtmyer. Survey of the stability of linear finite difference equations. *Communications on pure and applied mathematics*, 9(2):267–293, 1956.

[54] Joseph Abate and Ward Whitt. A unified framework for numerically inverting laplace transforms. *INFORMS Journal on Computing*, 18(4):408–421, 2006.

[55] Alan Talbot. The accurate numerical inversion of laplace transforms. *IMA Journal of Applied Mathematics*, 23(1):97–120, 1979.

[56] Tucker McClure. Numerical inverse laplace transform. https://uk.mathworks.com/matlabcentral/fileexchange/39035-numerical-inverse-laplace-transform. Accessed: 20/08/2019.

[57] Sky Sartorius. Bisection method root finding. https://uk.mathworks.com/matlabcentral/fileexchange/28150-bisection-method-root-finding. Accessed: 20/08/2019.

[58] Karen A Kopecky. Root-finding methods. *Economics*, 613:614, 2007.

[59] PA Vermeer and A Verruijt. An accuracy condition for consolidation by finite elements. *International Journal for numerical and analytical methods in geomechanics*, 5(1):1–14, 1981.

[60] Russell Charles Hibbeler. *Engineering mechanics*. Pearson education, 2001.

[61] Sunita Rani, Raman Kumar, and Sarva Jit Singh. A note on the effect of negative poisson's ratio on the deformation of a poroelastic half-space by surface loads. *Engineering*, 2(06):432, 2010.

[62] Alex Mogilner and Angelika Manhart. Intracellular fluid mechanics: Coupling cytoplasmic flow with active cytoskeletal gel. *Annual Review of Fluid Mechanics*, 50:347–370, 2018.

[63] MA Biot and DG Willis. The elastic coeff cients of the theory of consolidation. *J. appl. Mech*, 24:594–601, 1957.

[64] Bruce Roy Munson, Theodore Hisao Okiishi, Wade W Huebsch, and Alric P Rothmayer. *Fluid mechanics*. Wiley Singapore, 2013.

[65] Henry Philibert Gaspard Darcy. *Les Fontaines publiques de la ville de Dijon. Exposition et application des principes à suivre et des formules à employer dans les questions de distribution d'eau, etc.* V. Dalamont, 1856.

[66] W_F Brace, JB Walsh, and WT Frangos. Permeability of granite under high pressure. *Journal of Geophysical research*, 73(6):2225–2236, 1968.

[67] Rea Gauvin, F Trochu, Y Lemenn, and L Diallo. Permeability measurement and flow simulation through fiber reinforcement. *Polymer composites*, 17(1):34–42, 1996.

[68] Sean S Kohles, Julie B Roberts, Maureen L Upton, Christopher G Wilson, Lawrence J Bonassar, and Alyssa L Schlichting. Direct perfusion measurements of cancellous bone anisotropic permeability. *Journal of Biomechanics*, 34(9):1197–1202, 2001.

[69] Maxwell V Chor and Wei Li. A permeability measurement system for tissue engineering scaffolds. *Measurement Science and Technology*, 18(1):208, 2006.

[70] Edwin P Chan, Yuhang Hu, Peter M Johnson, Zhigang Suo, and Christopher M Stafford. Spherical indentation testing of poroelastic relaxations in thin hydrogel layers. *Soft Matter*, 8(5):1492–1498, 2012.

[71] Yuhang Hu, Xuanhe Zhao, Joost J Vlassak, and Zhigang Suo. Using indentation to characterize the poroelasticity of gels. *Applied Physics Letters*, 96(12):121904, 2010.

[72] Mario Borgnia, Søren Nielsen, Andreas Engel, and Peter Agre. Cellular and molecular biology of the aquaporin water channels. *Annual review of biochemistry*, 68(1):425–458, 1999.